Multi-Site Electrocatalysts Boost pH-Universal Nitrogen Reduction by High-Entropy Alloys

Dan Zhang[†‡], Huan Zhao[†], Xueke Wu[†], Ying Deng[†], Zuochao Wang[†], Yi Han[†], Hongdong Li[†], Yue Shi[†], Xilei Chen[‡], Shaoxiang Li[‡], Jianping Lai[†], Bolong Huang[§] and Lei Wang*[†‡]*

[†] D. Zhang, H. Zhao, X. Wu, Y. Deng, Z. Wang, Y. Han, H. Li, Y. Shi, Prof. J. Lai, Prof. L. Wang
Key Laboratory of Eco-chemical Engineering, Ministry of Education, Taishan scholar advantage and characteristic discipline team of Eco-chemical process and technology, Laboratory of Inorganic Synthesis and Applied Chemistry, College of Chemistry and Molecular Engineering, Qingdao University of Science and Technology, Qingdao 266042, P. R. China

[‡] D. Zhang, Prof. X. Chen, Prof. S. Li, Prof. L. Wang
Shandong Engineering Research Center for Marine Environment Corrosion and Safety Protection, College of Environment and Safety Engineering, Qingdao University of Science and Technology, Qingdao 266042, P. R. China

[§] Prof. B. Huang
Department of Applied Biology and Chemical Technology, The Hong Kong Polytechnic University, Hung Hom, Kowloon, Hong Kong SAR, China.

Keywords: high-entropy alloys; multi-site; NRR; electrocatalysis; pH-universal

Abstract:

Electrocatalytic nitrogen reduction reaction (NRR) has been an important area of research for many scientists. However, high voltage requirements, low NH_3 yield and poor stability remain the biggest challenges for NRR. Here, we report a novel high-entropy alloys (HEA) RuFeCoNiCu nanoparticles (NPs) with small size (~16 nm) and uniformity were prepared in oil phase at atmospheric pressure and low temperature (≤ 250°C) for the first time and applied them to NRR. According to the experiments, there is a high NH_3 yield at a low overpotential. When the test potential is 0.05 V *vs.* RHE in 0.1 M KOH, it has a surprising NH_3 yield of 57.1 μg h^{-1} mg^{-1}_{cat} (11.4 μg h^{-1} cm^{-2}), and the corresponding Faradaic efficiency (FE) reaches 38.5%, which is the electrocatalyst with the highest NH_3 yield at the voltage of 0.05 V *vs.* RHE reported so far. Similarly, the material also exhibits excellent electrochemical properties in other

electrolytes such as 0.1 M Li_2SO_4, 0.1 M Na_2SO_4 and 0.1 M HCl electrolytes. Besides, it also has an excellent electrochemical stability. After the 100 h test, only slightly diminished in activity. Density functional theory (DFT) shows that Fe surrounded by alloy metals is the best site for N_2 adsorption and activation. Co-Cu and Ni-Ru couples show an excellent capacity to surface hydrogenation at a low overpotential, in which case *H preferentially adsorbs on these sites. *H makes it easier to activate the adsorbed N_2 which from adjacent Fe with maximum energy input (0.32 eV), and finally reduced to NH_3.

1. Introduction

The development of the modern agricultural economy is inseparable from the use of ammonia. [1-3] Modern ammonia production methods are diverse. One of the methods is biological enzyme nitrogen fixation,[4,5] and the other is artificial nitrogen fixation using catalysts.[6,7] Using the Haber-Bosch process to convert the N_2 which accounts for 70% in the atmosphere into NH_3 is still the important backbone force for industrial ammonia production.[8,9] The high-temperature and high-pressure conditions make this process engender higher energy consumption and aggravate the greenhouse effect.[10-13] Later, new ammonia production methods appeared.[14-17] Electrocatalytic nitrogen reduction reaction (NRR) is a nitrogen fixation technology that generates NH_3 under relatively mild conditions using N_2 and water as raw materials.[18-20] It has become a new research hotspot in the field of electrocatalysis due to its environmentally friendly characteristics.[21,22] The central link of the electrocatalytic process is the preparation of high-efficiency catalysts. And a wide variety of effective electrocatalysts have emerged in the past few years.[23-33] Among them, transition metals play important roles in the progress of NRR and can be used to alleviate the kinetics issues of activating stronger N≡N bond.[34,35] However, the low NH_3 yield, high overpotential as well as poor stability remain the biggest challenges for NRR.

With the continuous advancement of materials science, new materials are constantly emerging. Through precisely controlling the coordination entropy, high-entropy alloys (HEAs) are synthesized by five or more metal elements with the same atomic ratio. [36,37] Due to the distinctive properties such as corrosion resistance under severe conditions and adjustable properties, HEA has received extensive attention from scientists. [38,39] Therefore, HEAs are expected to solve the above problems in NRR. At present, the commonly used HEAs synthesis mainly includes arc melting method, thermal carbon impact method, aerosol spray pyrolysis, melt spinning technology, ball milling and solvothermal method. Nevertheless, these methods not only often produce nanoparticles (NPs) with large average size (usually μm level) and irregular morphology but also face challenges such as complicated processes, high processing costs, or low yields. In addition, these processes often require high-temperature and high-pressure conditions. These limitations have hindered the practical usage of HEAs in various applications. [40] For the time being, there is no simple synthesis method under low temperature (≤ 250°C) and atmospheric pressure, and this type of material has not yet been applied to NRR.

In this article, we synthesized RuFeCoNiCu HEA NPs for the first time at low temperature (≤ 250°C) and atmospheric pressure and applied them to NRR. It was found that in 0.1 M KOH electrolyte, at a low overpotential (0.05 V *vs.* RHE), the NH_3 yield rate is 57.1 μg h^{-1} mg^{-1}_{cat} (11.4 μg h^{-1} cm^{-2}), and the Faradaic efficiency (FE) is 38.5%. Based on the comparison of the data reported so far (**Table S3**), it is the best material to boost NRR at 0.05 V *vs*. RHE. And this material also shows strikingly electrochemical properties in other electrolytes such as 0.1 M Li_2SO_4, 0.1 M Na_2SO_4 and 0.1 M HCl electrolytes. Besides, it exhibits excellent electrochemical stability. There was no significant attenuation in activity after 100 h test. Through computational screening, the surface of RuFeCoNiCu HEA has been examined by Monte-Carlo and density functional theory (DFT) approaches. Towards NRR, Fe in the alloy is considered the best site for N_2 adsorption and activation. Co-Cu and Ni-Ru couples have excellent

surface hydrogenation ability at low overpotential, forming *H on their surfaces. Rather than capturing protons directly from the solution, this source of H will more easily activate N_2 adsorbed on the adjacent Fe site with a maximum energy input of 0.32 eV and produce NH_3.

2. Results and Discussion

We synthesized RuFeCoNiCu HEA NPs for the first time at low temperature (≤ 250°C) and atmospheric pressure. During the experiment, the metal precursors were weighed and mixed at the same molar ratio, and then the reducing agent $Mo(CO)_6$ was added for further mixing. After adding oleylamine, ultrasonic mixing, the raw materials are fully dissolved in oleylamine and a transparent solution is formed (**Figure S1a**). In the oil bath process, with the increase of temperature and the extension of time, the transparent solution gradually turned black, which proved the occurrence of reduction and coordination fusion process (**Figure S1b**). As shown in **Figure 1a**, the synthesized material exhibited the size of particle concentrated about 15~16 nm (**Figure 1b**). X-ray diffraction (XRD) data show that only one significant diffraction peak at 43.0°, which was attributed to RuNi, (JCPDS No. 65-6490) (**Figure 1c**), indicating that there is only a single phase (hcp) instead of multiple phases. The XRD comparison of the RuFeCoNiCu and the premixed elements also proved the occurrence of the chemical reaction. From the high-resolution transmission electron micrograph (HRTEM), it was noted that the distance between two parallel lattices is 0.21 nm, which corresponds to the (002) crystal planes of RuNi (**Figure 1d**). The element mapping diagram of **Figure S2** just proves that all five elements uniformly distribute in this material. Inductively coupled plasma mass spectrometry (ICP-MS) analysis reveals that the ratio of RuFeCoNiCu is 22: 20: 18: 21: 19 (**Table S1**).

The state of each element in RuFeCoNiCu HEA NPs was investigated by X-ray photoelectron spectroscopy (XPS) spectrum. **Figure S3** shows detailed valence information for these five metal elements. In **Figure S3a**, the peaks locate around 280.1 eV and 284.4 eV belong to Ru^0 $3d_{5/2}$ and Ru^0 $3d_{3/2}$,

respectively. In **Figure S3b**, the peaks around 709.6 eV and 722.8 eV belong to Fe^0 $2p_{3/2}$ and Fe^0 $2p_{1/2}$. The peaks of 711.6 eV and 724.2 eV belong to Fe^{3+} $2p_{3/2}$ and Fe^{3+} $2p_{1/2}$. At the same time, these peaks are all positively shifted by about 0.3 eV, which proves that Fe may act as an electron donor to participate in the catalytic reaction. The peaks at 777.8 eV and 793.3 eV can be attributed to the Co^0 $2p_{3/2}$ and Co^0 $2p_{1/2}$. The peaks at 780.5 and 796.4 eV can be attributed to Co^{2+} $2p_{3/2}$ and Co^{2+} $2p_{1/2}$ (**Figure S3c**). The peaks at 854.0 eV and 873.0 eV can be attributed to the Ni^{2+} $2p_{3/2}$ and Ni^{2+} $2p_{1/2}$. The peaks at 852.3 and 869.7 eV can be attributed to Ni^0 $2p_{3/2}$ and Ni^0 $2p_{1/2}$ (**Figure S3d**). The peak at 932.2 eV corresponds to $2p_{3/2}$ of metallic Cu^0, and the peak at 952.5 eV belongs to Cu^0 $2p_{1/2}$ (**Figure S3e**). And there is no N element in this material (**Figure S4**). The element content obtained from XPS analysis is shown in **Table S2**. Due to the errors in the process of peak splitting and quantification, there are slight differences compared with ICP AES and EDS image (**Figure S5**). In addition, the thermodynamic parameters of RuFeCoNiCu HEA was evaluated. For multi-component synthetic alloys to form solid solution HEA, it is found that the formation of HEA often requires the following conditions: atomic size difference $\delta \leq 6.6\%$, $-11.6 < \Delta H_{mix} < 3.2$ (kJ mol^{-1}). In this work, we calculated the ΔH_{mix} of RuFeCoNiCu HEA is 0.77 kJ mol^{-1} and $\Delta S_{mix} =$ 13.35 J $K^{-1}mol^{-1}$, the atomic size difference is $\delta=2.15\% \leq 6.6\%$, and $\Delta G_{mix}= -5.8$ kJ mol^{-1}. Therefore, we guess that the RuFeCoNiCu HEA is a solid solution alloy.

We further explored the NRR activity of RuFeCoNiCu HEA NPs. Firstly, we prepared RuFeCoNiCu/C catalyst by combining the synthesized nanoparticles with Ketjen black (the mass ratio is 1:1) (**Figure S6**). We performed Temperature-programmed desorption of N_2 (N_2-TPD) on the RuFeCoNiCu/C (**Figure S7**). The peaks around 260°C and 345°C are the physical and chemical adsorption peaks of the RuFeCoNiCu/C, respectively, indicating that the RuFeCoNiCu/C has excellent physical and chemical adsorption capacity for N_2.[41,42] Then the catalyst was coated on 1×1 cm^2 carbon paper (RuFeCoNiCu/CP) to test the NRR activity in a 0.1 M KOH solution with a double cell electrolytic

cell. During the experiment, the N_2, electrolytic cell, and electrode surface passed through the decontamination process (see the Supporting Information for details).[43] As the principal product in this experiment, NH_3 was detected by a common indophenol blue method,[44] and the calibration curves are shown in the **Figure S8-11**. N_2H_4 may also be produced during the experiments, which is monitored by the Watt and Chrisp method,[45] and the calibration curve is shown in **Figure S12**. The pollutants in the gas are quantified by colorimetry after being treated with a copper catalyst to deduct the influence of pollutants (**Figure S13**). We carefully conducted several repeated tests on the linear sweep voltammograms (LSV) of N_2 and Ar at a fixed gas flow rate (10 mL min^{-1}) (**Figure 2a**). They all coincide with the original test curve, indicating that the difference between the LSV of N_2 and Ar is caused by NRR. And the results show a higher current density in the N_2-saturated electrolyte. Subsequently, a class of voltages were selected. The chronoamperometry experiments were performed at different potentials for 3600 s (**Figure 2b**). At the end of these experiments, the absorbance was detected by UV-Vis absorption spectra (**Figure 2c**), and the NH_3 concentration was calculated by the formula. The processed data are plotted as **Figure 2d**. When the overpotential is just only 0.05 V *vs.* RHE, it exhibits extraordinary NRR properties, the NH_3 yield is 57.1 μg h^{-1} mg^{-1}_{cat}, corresponding area yield is 11.4 μg h^{-1} cm^{-2} (**Figure S14**), and the FE is as high as 38.5%, which is far higher than the level reported in the literature. During the process of potential decay, as a consequence of competitive factors of HER possibly, NH_3 yields and FEs slowly decrease, but the numerical value still boasts a large advantage compared with the data reported in the literature (**Table S3**). What's more, the FEs of H_2 and NH_3 are listed in **Figure S15**, from which we can see clearly that RuFeCoNiCu/C possesses the most impressive NRR selectivity at 0.05 V *vs.* RHE. Moreover, the FE of NRR is lower than that of HER. Therefore, HER still occupies a dominant position in the catalysis process, and HER is suppressed. However, in this experiment, no by-product N_2H_4 was found (**Figure S16**). In addition to the UV-Vis detection method, we also quantitatively detect the NH_3

yield by ion chromatography (IC) (**Figure S17-18**). As shown in **Figure 3**, at 0.05 V *vs.* RHE, the NH_3 yield reached 56.7 μg h^{-1} mg^{-1}_{cat}, which is similar to the value detected by UV-Vis. We have quantified NH_3 production using the indophenol and IC methods, quantification using the NMR method with $^{14}N_2$ and $^{15}N_2$ has become one of the more convincing representations. We use the isotope labeling method to verify the results of this experiment. At the same time, we can also provide evidence for the source of N in the experiment. As shown in **Figure S19**, when $^{15}N_2$ is used as the N source, two signal peaks attributable to $^{15}NH_4^+$ are displayed. When $^{14}N_2$ is introduced as the N source, three signal peaks attributable to $^{14}NH_4^+$ are displayed. From the NMR standard curve **(Figure S20)**, we calculated that when $^{14}N_2$ and $^{15}N_2$ were used as N sources, the final NH_3 yields were almost consistent, and echoed the results obtained by colorimetry and IC (**Figure 3**). At the same time, this result also proves that the gas introduced in the experiment is the main N source and has an irreplaceable role in the experiment. We also tested the NRR properties of RuFeCoNiCu/CP at 0.05 V *vs.* RHE in 0.1 M Li_2SO_4, 0.1 M Na_2SO_4 and 0.1 M HCl electrolytes (**Figure S21**). It was found that the catalyst still has extraordinary NRR activity in 0.1 M Li_2SO_4, 0.1 M Na_2SO_4 and 0.1 M HCl electrolytes. The NH_3 yields are 52.6 μg h^{-1} mg^{-1}_{cat}, 47.2 μg h^{-1} mg^{-1}_{cat} and 37.1 μg h^{-1} mg^{-1}_{cat}, respectively. Corresponding FEs are 27.6%, 21.2% and 7.7%, respectively. The data disclose that RuFeCoNiCu/CP exhibits better NRR activity in 0.1 M KOH electrolyte compared with other electrolytes (**Figure S22**).

Catalyst stabilization is also an important factor in defining catalyst activity. In this experiment, we demonstrate the stability of RuFeCoNiCu/CP by various characterization tests. We continuously cycled the NRR test twelve times in N_2-saturated 0.1 M KOH and tested the NH_3 yields and FEs for each experiment (**Figure S23**). The data show that the catalyst maintains an efficient NRR efficiency after twelve cycles (**Figure 4a**). In addition, the NH_3 yield exhibits a linear correlation with the electrolysis time (**Figure 4b**). More notably, during the 100-h long-term electrolysis experiment, the time-current

curve doesn't show significant attenuation (**Figure 4c**), and the catalyst activity before and after the 100-hour reaction was not substantially reduced (**Figure 4d**), which all proved that RuFeCoNiCu/CP has excellent chemical stability. We also did a variety of comparative experiments to rule out the influencing factors other than RuFeCoNiCu/CP. As shown in **Figure S24a**, the NH_3 yield and FE on pure carbon paper are poor at 0.05 V *vs.* RHE, indicating that carbon paper has little effect on this experiment. At the same time, the effect of N_2 as the N source of this experiment was also studied (**Figure S24b**). In N_2 atmosphere, it exhibits satisfying NRR activity, while in Ar atmosphere, there is almost no activity, indicating that the N_2 in the experiment plays an important role in synthesizing NH_3. Furthermore, in the alternating experiments of N_2 and Ar (**Figure S25**), it is demonstrated that the high purity N_2 introduced was the main N element donor in this experiment. In addition, testing under open circuit potential under nitrogen is also necessary. This operation can explore the effect of contamination in the nitrogen gas flow on the experiment (**Figure S24**). We also detected the yield of NH_3 in Ar-saturated KOH solution. As expected, no obvious NH_3 peaks appeared during the detection **(Figure S26).** As shown in **Figure S27**, by changing the N_2 flow rate, the N_2 reduction efficiency under 0.05 V *vs.* RHE is stable without any significant change. After testing the electrochemical active surface area of RuFeCoNiCu/CP, it was found that this material has a large electrochemical double-layer capacitance (4.4 mF cm^{-2}) (**Figure S28**). In summary, the control experiments show that although the gas introduced and the experimental environment is completely treated, there will still be some impacts, but according to the NH_3 production, these impacts are minimal.

The RuFeCoNiCu/CP after the reaction was characterized by XRD, TEM and HRTEM (**Figure S29**). Even after a long period of reaction, the catalysts don't fall off from the Ketjen black, and the morphology and size don't change greatly. Besides, there was no obvious change in crystallinity. The XPS of Fe element after the reaction (**Figure S30**) shows that there was no obvious change. The ICP-MS test was

performed on the catalyst after the reaction, and the data show that the atomic ratio is still maintained. These all confirmed the awesome stability of RuFeCoNiCu/CP.

The quantitative results of ICP were considered in the actual calculation and modeling process. Because the Monte-Carlo method is used for corresponding random arrangement, this small difference in the content will not have a significant impact on the overall trend. The optimized HEA surface model was shown in **Figure 5**, where all the possible sites (including top, bridge and hollow) for N_2 molecule adsorption via side-on and end-on patterns were considered to screen in our calculations since the chemisorption of N_2 is essential to activate the inert N_2 molecule. **Figures S31-S34** are the optimized geometric configurations of the N_2 reduction reaction intermediates of b-Fe-Fe, h-Co-Ni-Ni, s-Ni-Ru and t-Fe, respectively. Moreover, the previous theoretical studies [46-48] suggested that the potential-determining step (PDS) on the NRR process is usually the first hydrogenation reaction of $*N_2+H\rightarrow *NNH$. Therefore, the Gibbs free energy changes of $\Delta G(*N_2)$ and $\Delta G(*N_2\text{-}*NNH)$ for the reaction steps of N_2 adsorption and addition of the first hydrogen on all of the possible positions were calculated and divided into four groups by the crossing lines of $\Delta G(N_2) = \Delta G(N_2\text{-}NNH) = 0.4$ eV in **Figure S35**. Obviously, the candidates presented in the left lower panel are the promising active sites for efficient NRR catalysis. Thus, the whole reaction processes in these positions were further investigated. Interestingly, as present in **Figure 5c-5f**, the PDS on each NRR process is not the first hydrogenation step, but $*NNH+H\rightarrow *NNH_2$ for t-Fe and h-Co-Ni-Ni sites, as well as the step of $*N+H\rightarrow *NH$ for b-Fe-Fe, with the largest Gibbs free energy changes of 0.32, 0.51 and 0.81 eV, respectively, which are lower than the values for all corresponding pure metals. A potential reason is that metals have been affected by neighboring atoms, showing a synergetic effect. For instance, t-Fe performs much better than pure Fe (111), whose thermodynamic barrier for PDS is around 1.0 eV. Metal-metal interaction and its effect on NRR can be also found from the Ni-Ru case. Specifically, when NRR occurs on the bridge site of Ni-Ru via side-on

model, N_2 adsorption and the first hydrogenation are exothermic steps, releasing 0.55 and 0.45 eV in Gibbs free energy, respectively. However, the addition of the second hydrogen via the enzymatic mechanism results in the largest uphill change of 1.98 eV in Gibbs free energy, as shown in **Figure 5d**. Releasing the first NH_3 molecule is rather feasible on the t-Fe, h-Co-Ni-Ni and b-Fe-Fe sites, due to the downhill energy changes, while a moderate uphill change of 0.52 eV in Gibbs free energy on the s-Ni-Ru site. However, the second NH_3 adsorption on the active sites is relatively strong, yielding the uphill Gibbs free energy changes of about 1.0 eV on the h-Co-Ni-Ni, b-Fe-Fe and s-Ni-Ru sites, except for the t-Fe site with the downhill energy change. From the calculation results of our previous work on high-entropy alloys,[49] it is known that the metal closer to the surface exhibits enhanced electrocatalytic electron transfer efficiency and enhanced electrical activity. The synergy of multiple active sites leads to the improvement of the final catalytic reaction performance. And as we all know, the higher the d-band center, the stronger the adsorption capacity.[50] From the d orbital partial density of states (PDOS) of each metal (**Figure S36**), it can be seen that the Fe site is closer to the Fermi level (E_F), so it is easier to combine with the catalytic substrate and has electron-rich characteristics, which is consistent with the results of XPS.

The added H on the N atom in the above process is not directly obtained from the solution. It is worth to investigate hydrogen adsorption H* over these active sites. Using $|\Delta G(H^*)|$ as an indicator, it is typically in the range of 0.3 to 0.6 eV in most cases on the surface; however, it is found that Co-Cu and Ni-Ru couples show an excellent capacity to surface hydrogenation **(Figure S37)** at a low overpotential with $\Delta G(H^*)$ being in the range of -0.2 ~ -0.3 eV,[51] in which case *H preferentially adsorbs on these sites. **Figure 5** shows that the hydrogenation process of t-Fe sites is more likely to occur, thereby inhibiting HER. So, when the coverage of *H on these sites is enough, the N_2 which from adjacent t-Fe is activated by the *H on the surface, and finally reduced to NH_3 (**Figure 6**). The optimal NRR voltage involved in this manuscript is 0.05 V *vs*. RHE. Under this ultra-low overpotential, the HER activity is very weak.

Moreover, the metal atom has a strong adsorption capacity for *H, which increases the reaction energy barrier for the formation of H_2 and inhibits HER. Comparing the FE of HER and NRR of RuFeCoNiCu/C, we found that although the NRR yield and FE are already excellent at 0.05 V *vs.* RHE, it can be found from **Figure S15** that the FE of HER is still higher than the FE of NRR. Therefore, HER is still the dominant reaction at this voltage.

We conducted a detailed theoretical study on how the catalyst inhibits HER. Among the four adsorption active sites listed in the manuscript, t-Fe and Co-Ni-Ni are the best and second-best catalytic sites for NRR, respectively. Among them, the adsorption energy of single H on t-Fe is -0.74 eV, which seems to occupy the active site of t-Fe and it is difficult to adsorb N_2. However, considering that the formation of H_2 requires the introduction of a second H, the top site adsorption is no longer stable due to the coverage effect of H adsorption at this time, and the two H atoms tend to be adsorbed at the hole position around t-Fe. The corresponding adsorption energy is as follows: (**Figure S38a**, unit eV). In the case of Co-Ni-Ni, it corresponds to the hole site, which corresponds to a single H adsorption energy of -0.38 eV. Once other H is adsorbed nearby, the adsorption energy will be further reduced to -0.26 eV. The coverage effect similar to the double adsorption of H-H can be observed in the other two active sites, such as Ni-Cu site (green solid circle) and t-Fe-Fe site (red hollow circle). The average adsorption energy of two H atoms is as **Figure S38b**. Compared with the original single H atom apical adsorption (Fe, Cu, Ni site adsorption energy is about -0.75 eV), the second H adsorption will reduce the H adsorption energy by about 0.2 eV. Based on the results of dihydrogen adsorption of the above four adsorption sites, it can be judged that when multiple H is adsorbed, it is mainly distributed in the hole position, and the adsorption energy decreases rapidly with the H coverage. Therefore, the surface H adsorption will affect the Co-Ni-Ni sites, but the optimal site of NRR, t-Fe, is not at the hole position and will not be significantly affected. Clearly, different metals may serve different roles and work in a synergetic way to bring excellent NRR

performance. Moreover, HEA can shorten the distance between active sites [52] and provide a huge space for component optimization, advanced knowledge for such a synergetic role between metals can greatly help the rational design of catalysts.

3. Conclusion

In summary, we have synthesized RuFeCoNiCu HEA NPs for the first time at low temperature (≤ 250°C) and atmospheric pressure. This is the first time that HEA used for boosting NRR. RuFeCoNiCu/CP has strikingly NRR properties in 0.1 M KOH solution, with 57.1 μg h^{-1} mg^{-1}_{cat} (11.4 μg h^{-1} cm^{-2}) NH_3 yield at 0.05 V *vs.* RHE, and FE up to 38.5%. It also shows excellent NRR activity in 0.1 M Li_2SO_4, 0.1 M Na_2SO_4 and 0.1 M HCl electrolytes. What's more, RuFeCoNiCu/CP has exceptional stability. After the 100-h test, only slightly diminished in activity. DFT-based screening has shown that t-Fe, b-Fe-Fe, h-Co-Ni-Ni and s-Ni-Ru are four promising sites, and t-Fe as the best from free energy calculations for full NRR. Co-Cu and Ni-Ru couples have shown excellent capacity to surface hydrogenation at low overpotential, with ΔG(H*) being in the range of -0.2 ~ -0.3 eV, in which case *H may firstly adsorb over these sites. When the coverage of *H on these sites is sufficiently large, the N_2 which from t-Fe is activated by the *H on the surface, and finally reduced to NH_3. Synergetic roles between alloy elements have been identified as a key reason for observed performance offered by high-entropy alloy. This research not only provides a new method for HEAs synthesis, but also expands its application to the field of NRR, demonstrating a new NRR mechanism.

Supporting Information.

Supporting Information is available from the Wiley Online Library or from the author.

Corresponding Authors

*(J.L.) E-mail: jplai@qust.edu.cn.

*(L.W.) E-mail: inorchemwl@126.com.

Conflict of Interest

The authors declare no conflict of interest.

Acknowledgment

This work was supported by the National Natural Science Foundation of China (51772162, 51802171), the Taishan Scholars program, Natural Science Foundation of Shandong Province, China (ZR2018BB031), Youth Innovation of Shandong Higher Education Institutions, China (2019KJC004), Outstanding Youth Foundation of Shandong Province, China (ZR2019JQ14), the Taishan Scholar Project of Shandong Province (tsqn201909123).

Received: ((will be filled in by the editorial staff))

Revised: ((will be filled in by the editorial staff))

Published online: ((will be filled in by the editorial staff))

References

[1] J. G. Chen, R. M. Crooks, L. C. Seefeldt, K. L. Bren, R. M. Bullock, M. Y. Darensbourg, P. L. Holland, B. Hoffman, M. J. Janik, A. K. Jones, M. G. Kanatzidis, P. King, K. M. Lancaster, S. V. Lymar, P. Pfromm, W. F. Schneider, R. R. Schrock, *Science* **2018**, *360*, eaar6611.

[2] C. Tang, S.-Z. Qiao, *Chem. Soc. Rev.* **2019**, *48*, 3166-3180.

[3] W. Tong, B. Huang, P. Wang, L. Li, Q. Shao, X. Huang, *Angew. Chem. Int. Ed.* **2020**, *59*, 2649-2653.

[4] B. K. Burgess, D. J. Lowe, *Chem. Rev.* **1996**, *96*, 2983-3012.

[5] B. M. Hoffman, D. Lukoyanov, Z.-Y. Yang, D. R. Dean, L. C. Seefeldt, *Chem. Rev.* **2014**, *114*, 4041-4062.

[6] Y. Li, Y. Li, B. Wang, Y. Luo, D. Yang, P. Tong, J. Zhao, L. Luo, Y. Zhou, S. Chen, F. Cheng, J. Qu, *Nat. Chem.* **2013**, *5*, 320-326.

[7] S. F. McWilliams, P. L. Holland, *Acc. Chem. Res.* **2015**, *48*, 2059-2065.

[8] S.-J. Li, D. Bao, M.-M. Shi, B.-R. Wulan, J.-M. Yan, Q. Jiang, *Adv. Mater.* **2017**, *29*, 1700001.

[9] D. Bao, Q. Zhang, F.-L. Meng, H.-X. Zhong, M.-M. Shi, Y. Zhang, J.-M. Yan, Q. Jiang, X.-B. Zhang, *Adv. Mater.* **2017**, *29*, 1604799.

[10] C. X. Guo, j. Ran, A. Vasileff, S. Qiao, *Energy Environ. Sci.* **2018**, *11*, 45-56.

[11] G.-F. Chen, X. Cao, S. Wu, X. Zeng, L.-X. Ding, M. Zhu, H. Wang, *J. Am. Chem. Soc.* **2017**, *139*, 9771-9774.

[12] Y. Tanabe, Y. Nishibayashi, *Coordin. Chem. Rev.* **2013**, *257*, 2551-2564.

[13] R. Michalsky, A. M. Avram, B. A. Peterson, P. H. Pfromm, A. A. Peterson, *Chem. Sci.* **2015**, *6*, 3965-3974.

[14] K. A. Brown, D. F. Harris, M. B. Wilker, A. Rasmussen, N. Khadka, H. Hamby, S. Keable, G. Dukovic, J. W. Peters, L. C. Seefeldt, P. W. King, *Science* **2016**, *352*, 448-450.

[15] M. Ali, F. Zhou, K. Chen, C. Kotzur, C. Xiao, L. Bourgeois, X. Zhang, D. R. MacFarlane, *Nat. Commun.* **2016**, *7*, 11335.

[16] A. Banerjee, B. D. Yuhas, E. A. Margulies, Y. Zhang, Y. Shim, M. R. Wasielewski, M. G. Kanatzidis, *J. Am. Chem. Soc.* **2015**, *137*, 2030-2034.

[17] H.-B. XPSWang, J.-Q. Wang, R. Zhang, C.-Q. Cheng, K.-W. Qiu, Y.-j. Yang, J. Mao, H. Liu, M. Du, C.-K. Dong, X.-W. Du, *ACS Catal.* **2020**, *10*, 4914-4921.

[18] Y. Luo, G.-F. Chen, L. Ding, X. Chen, L.-X. Ding, H. Wang, *Joule* **2018**, *3*, 279-289.

[19] D. Yan, H. Li, C. Chen, Y. Zou, S. Wang, *Small Methods* **2019**, *3*, 1800331.

[20] S. Zhao, X. Lu, L. Wang, J. Gale, R. Amal, *Adv. Mater.* **2019**, *31*, 1805367.

[21] Y.-X. Lin, S.-N. Zhang, Z.-H. Xue, J.-J. Zhang, H. Su, T.-J. Zhao, G.-Y. Zhai, X.-H. Li, M. Antonietti, J.-S. Chen, *Nat. Commun.* **2019**, *10*, 4380.

[22] X. Liu, Y. Jiao, Y. Zheng, M. Jaroniec, S.-Z. Qiao, *J. Am. Chem. Soc.* **2019**, *141*, 9664-9672.

[23] L. M. Azofra, N. Li, D. R. MacFarlane, C. Sun, *Energy Environ. Sci.* **2016**, *9*, 2545-2549.

[24] C. He, Z.-Y. Wu, L. Zhao, M. Ming, Y. Zhang, Y. Yi, J.-S. Hu, *ACS Catal.* **2019,** *9*, 7311-7317.

[25] M. M. Shi, D. Bao, S. J. Li, B. R. Wulan, J. M. Yan, Q. Jiang, *Adv. Energy Mater.* **2018**, *8*, 1800124.

[26] X. Wu, Z. Wang, Y. Han, D. Zhang, M. Wang, H. Li, H. Zhao, Y. Pan, J. Lai, L. Wang, *J. Mater. Chem. A* **2020**, *8*, 543-547.

[27] J. Zhang, X. Tian, M. Liu, H. Guo, J. Zhou, Q. Fang, Z. Liu, Q. Wu, J. Lou, *J. Am. Chem. Soc.* **2019**, *141*, 19269-19275.

[28] N. Cao, Z. Chen, K. Zang, J. Xu, J. Zhong, J. Luo, X. Xu, G. Zheng, *Nat. Commun.* **2019**, *10*, 2877.

[29] Q. Qin, Y. Zhao, M. Schmallegger, T. Heil, J. Schmidt, R. Walczak, G. Gescheidt-Demner, H. Jiao, M. Oschatz, *Angew. Chem. Int. Ed.* **2019**, *58,* 13101-13106.

[30] X. Yang, S. Kattel, J. Nash, X. Chang, J. Lee, Y. Yan, J. Chen, B. Xu, *Angew. Chem. Int. Ed.* **2019**, *58*, 13768-13772.

[31] G. Zhang, Q. Ji, K. Zhang, Y. Chen, Z. Li, H. Liu, J. Li, J. Qu, *Nano Energy* **2019**, *59*, 10-16.

[32] L. Hui, Y. Xue, H. Yu, Y. Liu, Y. Fang, C. Xing, B. Huang, Y. Li, *J. Am. Chem. Soc.* **2019**, *141*, 10677-10683.

[33] J. Han, Z. Liu, Y. Ma, G. Cui, F. Xie, F. Wang, Y. Wu, S. Gao, Y. Xu, X. Sun, *Nano Energy* **2018**, *52*, 264-270.

[34] H.-P. Jia, E. A. Quadrelli, *Chem. Soc. Rev.* **2014**, *43*, 547-564.

[35] Y. Yao, S. Zhu, H. Wang, H. Li, M. Shao, *J. Am. Chem. Soc.* **2018,** *140*, 1496-1501.

[36] J.-W. Yeh, S. K. Chen, S.-J. Lin, J.-Y. Gan, T.-S. Chin, T. Shun, C. H. Tsau, S. Y. Chang, *Adv. Eng. Mater.* **2004**, *6*, 299-303.

[37] M. W. Glasscott, A. D. Pendergast, S. Goines, A. R. Bishop, A. T. Hoang, C. Renault, J. E. Dick, *Nat. Commun.* **2019**, *10*, 2650.

[38] R. Liu, H. Chen, Z. Kunpeng, Y. Qin, B. Jiang, T. Zhang, G. Sha, X. Shi, C. Uher, W. Zhang, L. Chen, *Adv. Mater.* **2017**, *29*, 1702712.

[39] D. B. Miracle, O. N. Senkov, *Acta Mater.* **2017**, *122*, 448-511.

[40] V. Soare, M. Burada, I. Constantin, D. Mitrică, V. Bădiliţă, A. Caragea, M. Târcolea, *Appl. Surf. Sci.* **2015**, *358*, 533-539.

[41] Y. Wang, X. Cui, J. Zhao, G. Jia, L. Gu, Q. Zhang, L. Meng, Z. Shi, L. Zheng, C. Wang, Z. Zhang, W. Zheng, *ACS Catal.* **2018**, *9*, 336-344.

[42] Z.-H. Xue, S.-N. Zhang, Y.-X. Lin, H. Su, G.-Y. Zhai, J.-T. Han, Q.-Y. Yu, X.-H. Li, M. Antonietti, J.-S. Chen, *J. Am. Chem. Soc.* **2019**, *141*, 14976-14980.

[43] S. Z. Andersen, V. Čolić, S. Yang, J. A. Schwalbe, A. C. Nielander, J. M. McEnaney, K. Enemark-Rasmussen, J. G. Baker, A. R. Singh, B. A. Rohr, M. J. Statt, S. J. Blair, S. Mezzavilla, J. Kibsgaard, P. C. K. Vesborg, M. Cargnello, S. F. Bent, T. F. Jaramillo, I. E. L. Stephens, J. K. Nørskov, I. Chorkendorff, *Nature* **2019,** *570*, 504-508.

[44] D. Zhu, L. Zhang, R. E. Ruther, R. J. Hamers, *Nat. Mater.* **2013**, *12*, 836-841.

[45] G. W. Watt, J. D. Chrisp, *Anal. Chem.* **1952**, *24*, 2006-2008.

[46] J. Zhao, Z. Chen, *J. Am. Chem. Soc.* **2017**, *139*, 12480-12487.

[47] L. Li, X. Wang, H. Guo, G. Yao, H. Yu, Z. Tian, B. Li, L. Chen, *Small Methods* **2019**, *3*, 1900337.

[48] C. Ling, Y. Ouyang, Q. Li, X. Bai, X. Mao, A. Du, J. Wang, *Small Methods* **2019**, *3*, 1800376.

[49] H. Li, Y. Han, H. Zhao, W. Qi, D. Zhang, Y. Yu, W. Cai, S. Li, J. Lai, B. Huang, L. Wang, *Nat. Commun*. **2020**, *11*, 5437.

[50] J. Wang, B. Huang, Y. Ji, M. Sun, T. Wu, R. Yin, X. Zhu, Y. Li, Q. Shao, X. Huang, *Adv. Mater.* **2020**, *32*, 1907112.

[51] C. Ling, Y. Zhang, Q. Li, X. Bai, L. Shi, J. Wang, *J. Am. Chem. Soc.* **2019**, *141*, 18264-18270.

[52] G. Hu, L. Shang, T. Sheng, Y. Chen, L. Wang, *Adv. Funct. Mater.* **2020**, *30*, 2002281.

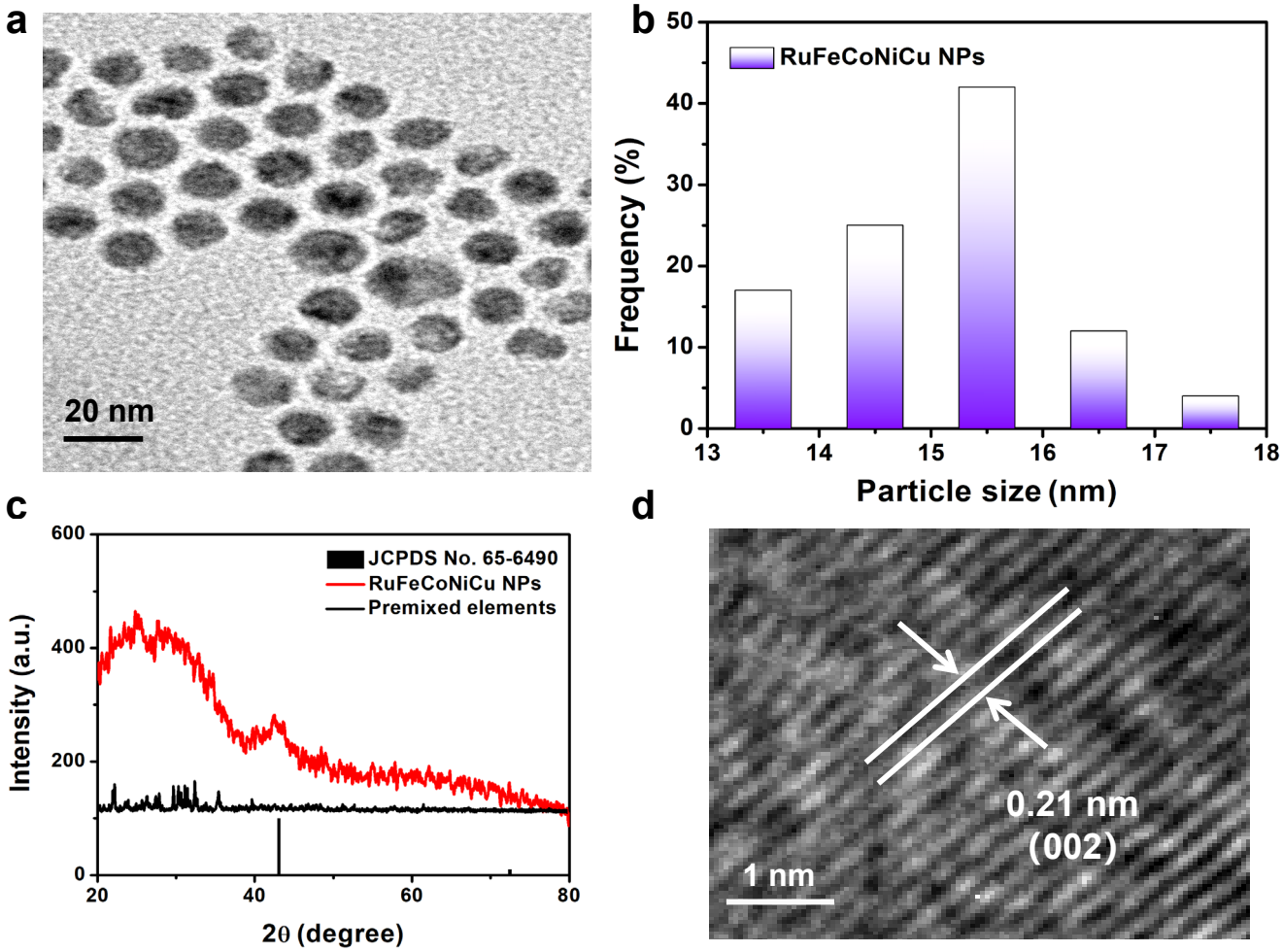

Figure 1. (a) TEM image of RuFeCoNiCu NPs. (b) Particle size distribution of RuFeCoNiCu NPs. (c) XRD pattern of premixed elements and RuFeCoNiCu NPs. (d) HRTEM images of RuFeCoNiCu NPs.

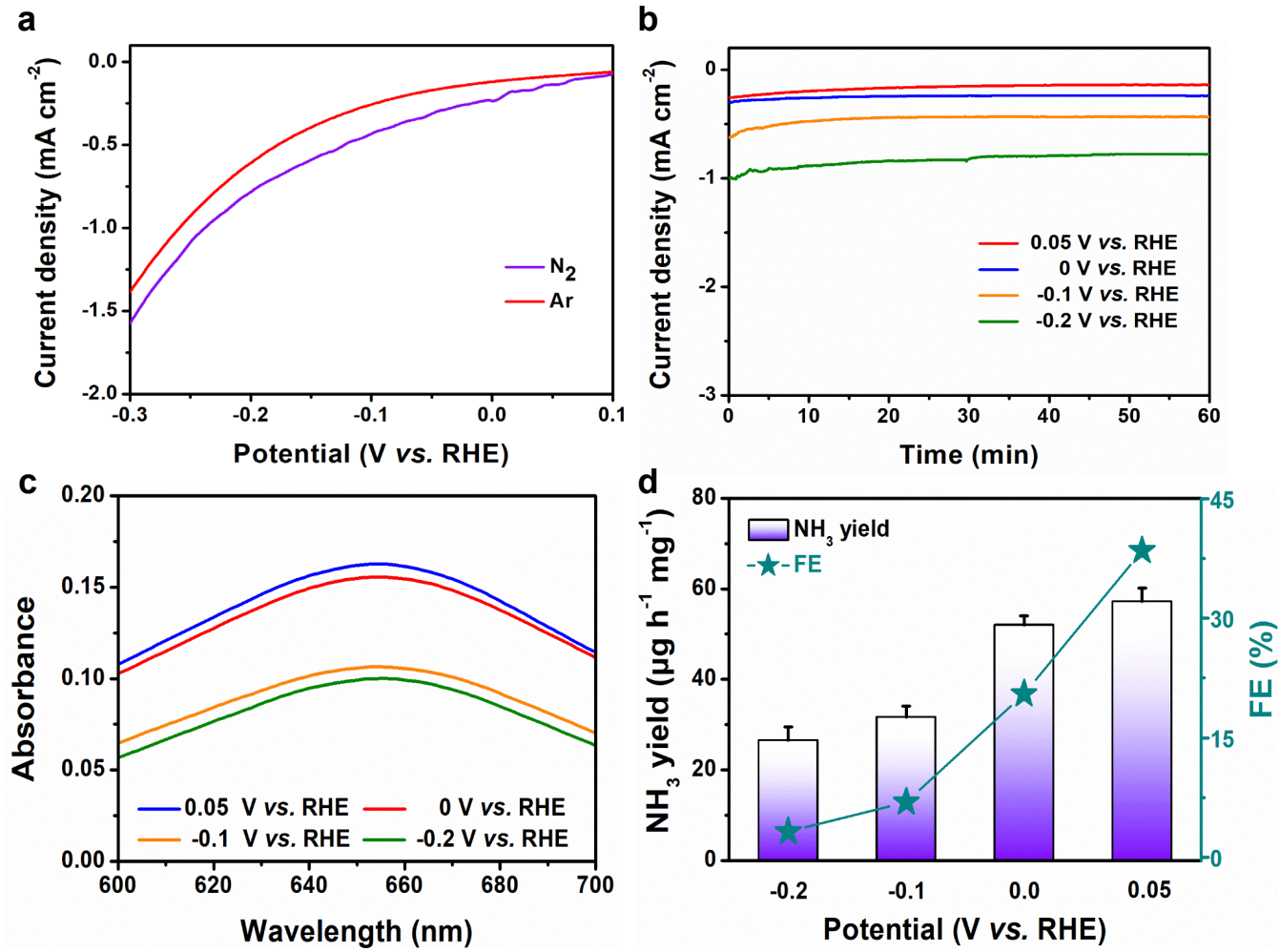

Figure 2. (a) LSV curves of RuFeCoNiCu/CP in N_2- and Ar-saturated 0.1 M KOH with a scan rate of 5 mV s^{-1}. (b) Time-dependence current density curves at various potentials in N_2-saturated 0.1 M KOH. (c) UV-Vis absorption spectra of the 0.1 M KOH electrolytes stained with indophenol indicator after 1 h electrolysis under N_2 at each given potential. (d) NH_3 yields and FEs at each given potential in 0.1 M KOH.

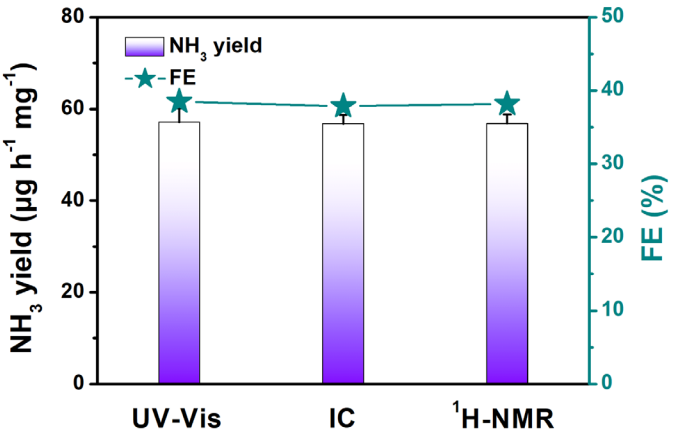

Figure 3. The yield of NH_3 for RuFeCoNiCu/CP at 0.05 V *vs.* RHE characterized by UV-Vis, IC and ^{1}H-NMR.

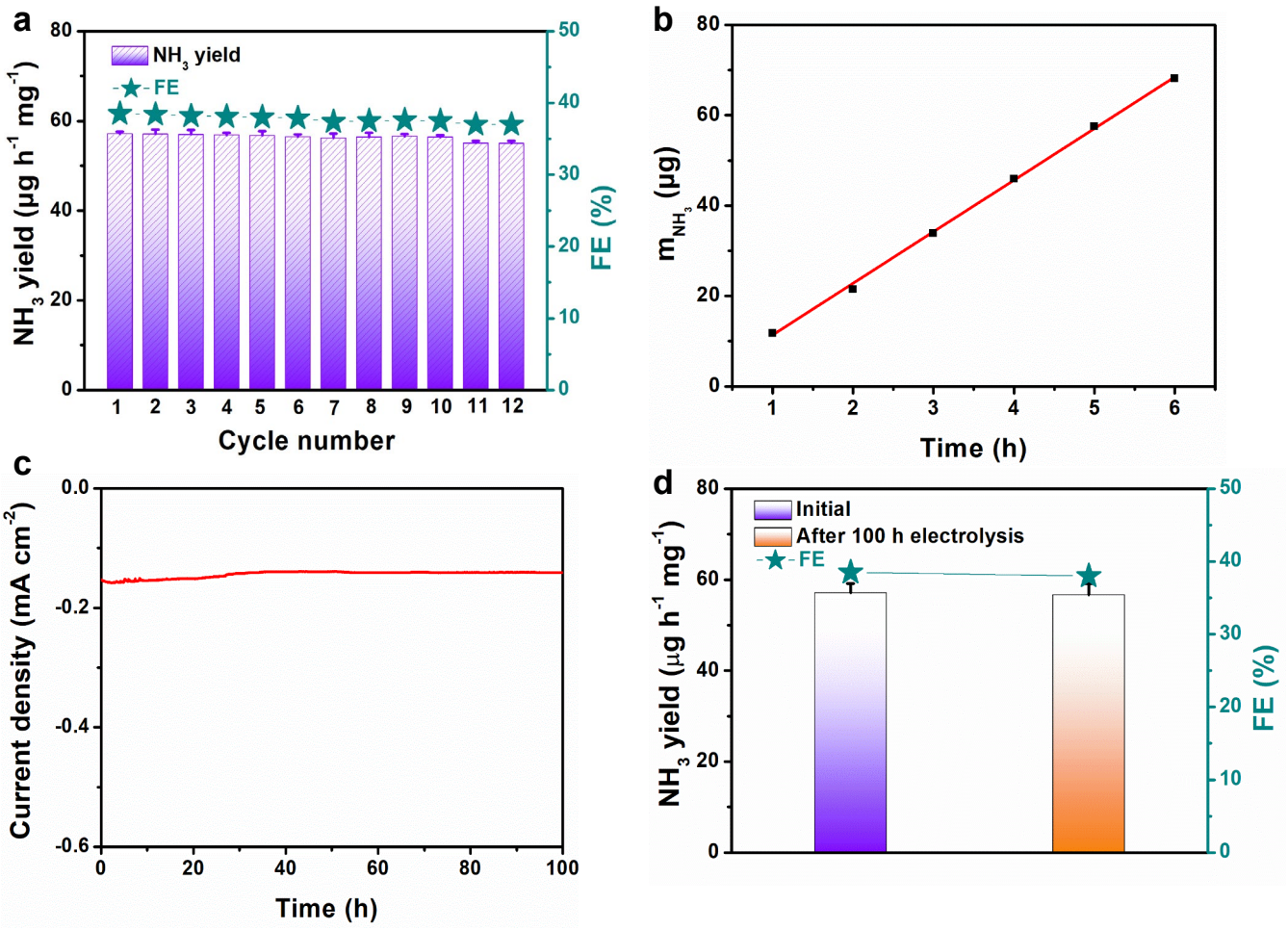

Figure 4. (a) NH_3 yields and FEs at 0.05 V *vs.* RHE during recycling test for 12 times. (b) The curve of NH_3 production *vs.* reaction time at 0.05 V *vs.* RHE over RuFeCoNiCu/CP. (c) Time-dependent current density curve for RuFeCoNiCu/CP at the potential of 0.05 V *vs.* RHE. (d) NH_3 yields and FEs after reacting at 0.05 V *vs.* RHE for 1 h and 100 h.

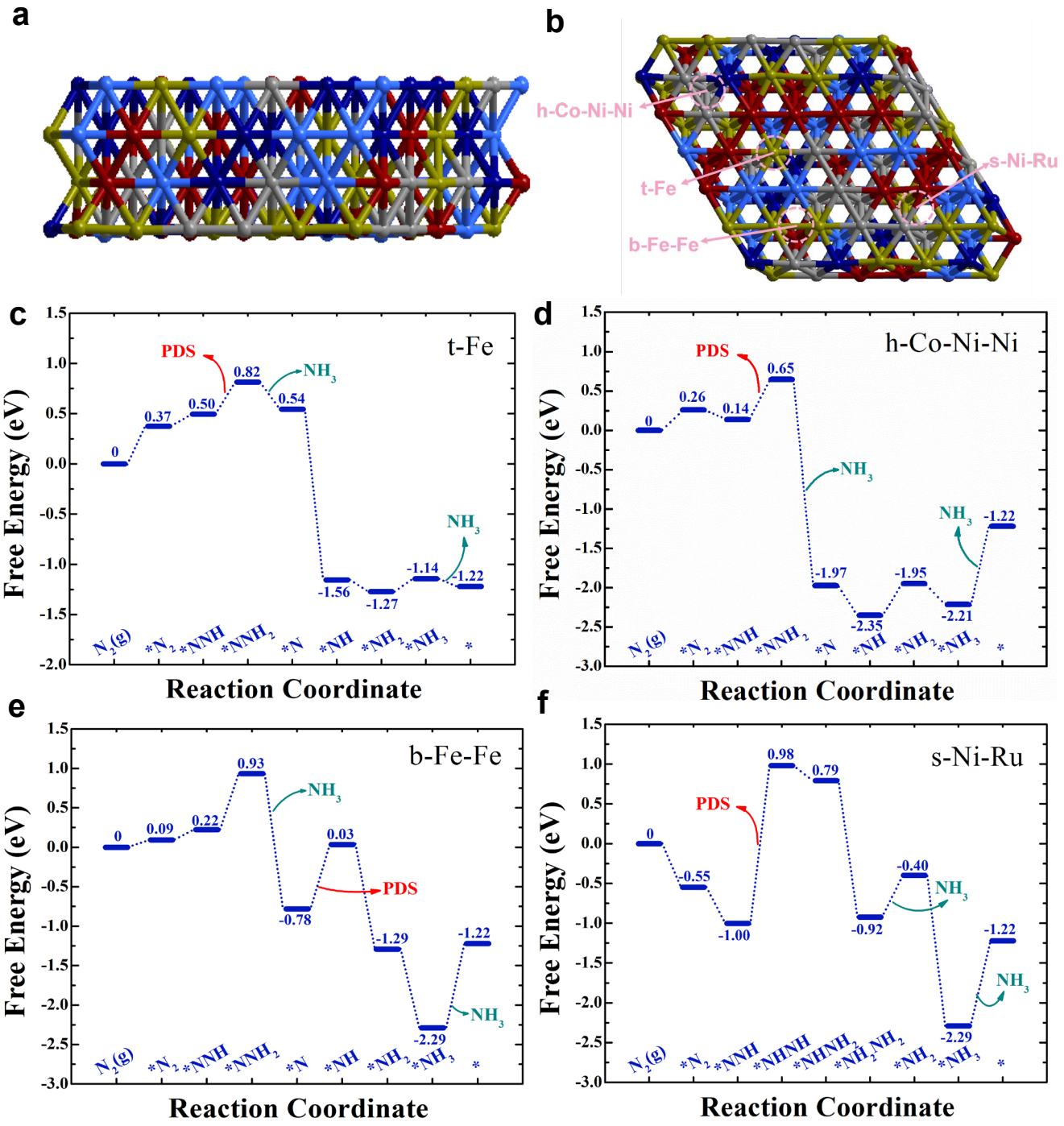

Figure 5. The optimized structure of the RuFeCoNiCu NPs. The red, yellow, dark blue, light blue and grey balls represent Ru, Fe, Co, Cu and Ni atoms, respectively. (a) side view; (b) top view with the network. Free energy diagrams for NRR process occurring on the (c) t-Fe, (d) h-Co-Ni-Ni, (e) b-Fe-Fe and (f) s-Ni-Ru sites. An asterisk (*) denotes as the adsorption site.

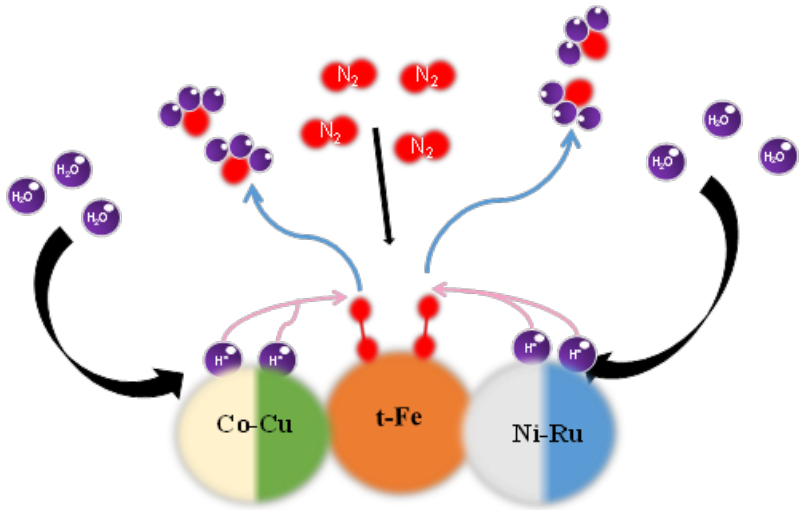

Figure 6. Schematic illustration of a possible mechanism to explain the enhanced NRR activity of RuFeCoNiCu NPs at low overpotential.

The table of contents entry

RuFeCoNiCu HEA NPs were synthesized at low temperature (≤ 250°C) and atmospheric pressure for the first time and used for boosting NRR. DFT shows that the synergetic roles between alloy elements have been identified as a key reason for observed performance offered by high-entropy alloy at low overpotential.

Keyword: high-entropy alloys; multi-site; NRR; electrocatalysis; pH-universal

Dan Zhang[†‡], Huan Zhao[†], Xueke Wu[†], Ying Deng[†], Zuochao Wang[†], Yi Han[†], Hongdong Li[†], Yue Shi[†], Xilei Chen[‡], Shaoxiang Li[‡], Jianping Lai*[†], Bolong Huang[§] and Lei Wang*[†‡]

Multi-Site Electrocatalysts Boost pH-Universal Nitrogen Reduction by High-Entropy Alloys